

JGR Earth Surface

RESEARCH ARTICLE

10.1029/2020JF005858

Key Points:

- Hilltop curvature at our sites does not vary linearly with erosion rate, as predicted by theory
- The inferred transport coefficient appears to be insensitive to climate
- Processes affecting the underlying bedrock may control the shape of soil-mantled hillslopes

Correspondence to:

E. J. Gabet,
manny.gabet@sjsu.edu

Citation:

Gabet, E. J., Mudd, S. M., Wood, R. W., Grieve, S. W. D., Binnie, S. A., & Dunai, T. J. (2021). Hilltop curvature increases with the square root of erosion rate. *Journal of Geophysical Research: Earth Surface*, 126, e2020JF005858. <https://doi.org/10.1029/2020JF005858>

Received 28 AUG 2020

Accepted 8 APR 2021

Hilltop Curvature Increases With the Square Root of Erosion Rate

E. J. Gabet¹ , S. M. Mudd² , R. W. Wood¹, S. W. D. Grieve³ , S. A. Binnie⁴, and T. J. Dunai⁴

¹Department of Geology, San Jose State University, San Jose, CA, USA, ²School of Geosciences, University of Edinburgh, Edinburgh, UK, ³School of Geography, Queen Mary University of London, London, UK, ⁴Institute for Geology and Mineralogy, University of Cologne, Cologne, Germany

Abstract The shape of soil-mantled hillslopes is typically attributed to erosion rate and the transport efficiency of the various processes that contribute to soil creep. While climate is generally hypothesized to have an important influence on soil creep rates, a lack of uniformity in the measurement of transport efficiency has been an obstacle to evaluating the controls on this important landscape parameter. We addressed this problem by compiling a data set in which the transport efficiency has been calculated using a single method, the analysis of hilltop curvatures using 1-m LiDAR data, and the erosion rates have also been determined via a single method, in-situ cosmogenic ¹⁰Be concentrations. Moreover, to control for lithology, we chose sites that are only underlain by resistant bedrock. The sites span a range of erosion rates (6–922 mm/kyr), mean annual precipitation (39–320 cm/yr), and aridity index (0.08–1.38). Surprisingly, we find that hilltop curvature varies with the square root of erosion rate, whereas previous studies predict a linear relationship. In addition, we find that the inferred transport coefficient also varies with the square root of erosion rate but is insensitive to climate. We explore various mechanisms that might link the transport coefficient to the erosion rate and conclude that present theory regarding soil-mantled hillslopes is unable to explain our results and is, therefore, incomplete. Finally, we tentatively suggest that processes occurring in the bedrock (e.g., fracture generation) may play a role in the shape of hillslope profiles at our sites.

1. Introduction

On soil-mantled surfaces too gentle for significant landsliding, particles are primarily transported downslope by soil creep. Soil creep is a general term for the cumulative effect of myriad individual processes that locally disturb soil, such as the freezing and thawing of pore water (R. S. Anderson et al., 2013), shrink-swell cycles (Carson & Kirkby, 1972), dry ravel (H. W. Anderson et al., 1959; Gabet, 2003), burrowing by animals (Gabet et al., 2003), and tree throw (e.g., Denny & Goodlett, 1956). Culling (1963) proposed that the rate of soil creep (q_s ; L^2/T) is linearly proportional to hillslope gradient, S (L/L), such that

$$q_s = DS \quad (1)$$

where D (L^2/T) is a sediment transport coefficient. The sediment transport coefficient, D , is a measure of the efficiency of the various soil creep processes, and its magnitude sets the pace for hillslope evolution (e.g., Fernandes & Dietrich, 1997; Roering et al., 1999). Although a nonlinear relationship between gradient and flux is supported by topographic analysis (Andrews & Bucknam, 1987; Grieve et al., 2016; Hurst et al., 2012; Roering et al., 1999) and physical simulations (Gabet, 2000; Roering, Kirchner, Sklar, & Dietrich, 2001), this relationship reduces to Equation 1 on slopes $<20^\circ$ (Hurst et al., 2012).

Our understanding of the controls on D for a particular landscape is limited. Because soil creep processes are typically climatically controlled, either directly (e.g., freeze-thaw) or indirectly through climate's effect on the distribution of the biota, temperature and precipitation are expected to have a dominant role in the transport efficiency of soil creep (e.g., Dunne et al., 2010; Hanks, 2000; Pelletier et al., 2011). Indeed, Hurst et al. (2013) and Richardson et al. (2019) found that D increases with mean annual precipitation, albeit weakly; the latter also found that D increases with the aridity index, which is the ratio between precipitation and evapotranspiration (Trabucco & Zomer, 2019). In contrast, Ben-Asher et al. (2017) concluded that transport efficiency decreases with precipitation, although this result was based on a small data set. Soil thickness (Furbish et al., 2009; Heimsath et al., 2005) and soil texture (Furbish et al., 2009), as well as the

underlying lithology (Hurst et al., 2013), may also be important factors. A lack of uniformity in measuring D , however, has been an obstacle in investigating the effect of these various factors.

Determining the controls on the transport coefficient is important for a variety of reasons. Because many landscapes are soil-mantled, not affected by overland flow, and too gentle for significant landsliding, Equation 1 and its nonlinear counterpart are thought to offer a complete description (or nearly so) of sediment transport across much of the Earth's surface. Moreover, assuming steady state topography, combining Equation 1 with a statement of mass conservation yields

$$C_{HT} = -\frac{E}{D} \left(\frac{\rho_s}{\rho_r} \right) \quad (2)$$

where E is the erosion rate (L/T), C_{HT} (1/L) is the two-dimensional curvature (i.e., the Laplacian of elevation) of a hill's ridge crest, and ρ_s and ρ_r are the density (L³/T) of soil and rock, respectively (Roering et al., 2007). With this equation (and its nonlinear version), D and E are both assumed to be independent variables: E is controlled by the rate at which the lower boundary is lowered (e.g., via river incision in response to uplift), and D is controlled by the intensity of the various soil creep processes. According to this theory, the profile of a hillslope adjusts itself such that its curvature satisfies Equation 2 (Culling, 1963; Gilbert, 1909). Therefore, understanding the controls on the transport efficiency should provide insight into the hillslope form. In addition, studies have used Equation 1 and its nonlinear version to model the degradation of fault scarps to estimate the earthquake recurrence interval (e.g., Hanks & Schwartz, 1987), and the results are sensitive to the value of the transport coefficient. Finally, understanding the role of the various factors on D is important as geologists attempt to infer erosion rates based on topographic analyses (Hurst et al., 2012).

2. Methods

2.1. Site Selection and Descriptions

Appropriate sites were limited to watersheds which had both LiDAR and cosmogenic ¹⁰Be data sets. The ¹⁰Be data came from a global compilation (Harel et al., 2016), and the associated LiDAR data were acquired from the OpenTopography (<http://opentopo.sdsc.edu>) and USGS (<https://viewer.nationalmap.gov>) platforms. LiDAR data with spatial resolutions coarser than 1-m cannot accurately resolve ridgeline curvatures in all settings (Grieve et al., 2016) and so any sites without 1-m resolution data were excluded from the analysis. Because ridgeline curvatures were used to estimate D (see below), only watersheds that appeared to be in topographic steady state were chosen. For example, watersheds with clear knickpoints or with asymmetrical ridges were avoided, as well as steep watersheds advancing into low-relief surfaces. Simulations of hillslope evolution suggest that hillslopes with declining erosion rates adjust so quickly that they are difficult to differentiate from steady state hillslopes; furthermore, hillslopes experiencing accelerated uplift only preserve the signature of changing erosion rates for tens of thousands of years (Mudd, 2017). Therefore, by avoiding areas with obvious signs of landscape transience, we are less likely to find ridge-line curvatures reflective of transient conditions. Thirty sites from six regions in the United States met our criteria: the Olympic Peninsula (WA; Belmont et al., 2007), the Feather River area (CA; Hurst et al., 2012; Riebe et al., 2001; Saucedo & Wagner, 1992), the San Gabriel Mountains (CA; DiBiase et al., 2010), Yucaipa Ridge (CA; Binnie et al., 2007), the Idaho Plateau (ID; Wood, 2013), and the Blue Ridge Mountains (VA; Duxbury, 2009; Figure 1). Some of the regions (e.g., the San Gabriel Mountains) had ¹⁰Be data for sites not covered by available LiDAR data and thus, their full data sets could not be used. Climatic data for these sites were obtained from the 800-m resolution PRISM model (PRISM, 2014), which provides recent (1981–2010) 30-year means for annual precipitation (MAP) and annual temperature (MAT; Table 1). The aridity index for the sites was determined from Trabucco and Zomer (2019). While these data are for the modern climate, we assume that they are representative (at least in a relative sense) of the climate state over the timescale of the erosion rates measured with ¹⁰Be (i.e., 10³–10⁵ yrs). To control for rock strength, we chose sites underlain by lithologies known to be resistant to erosion: plutonic and metamorphic bedrock (e.g., Gabet, 2020; Hack, 1973; Table 1).

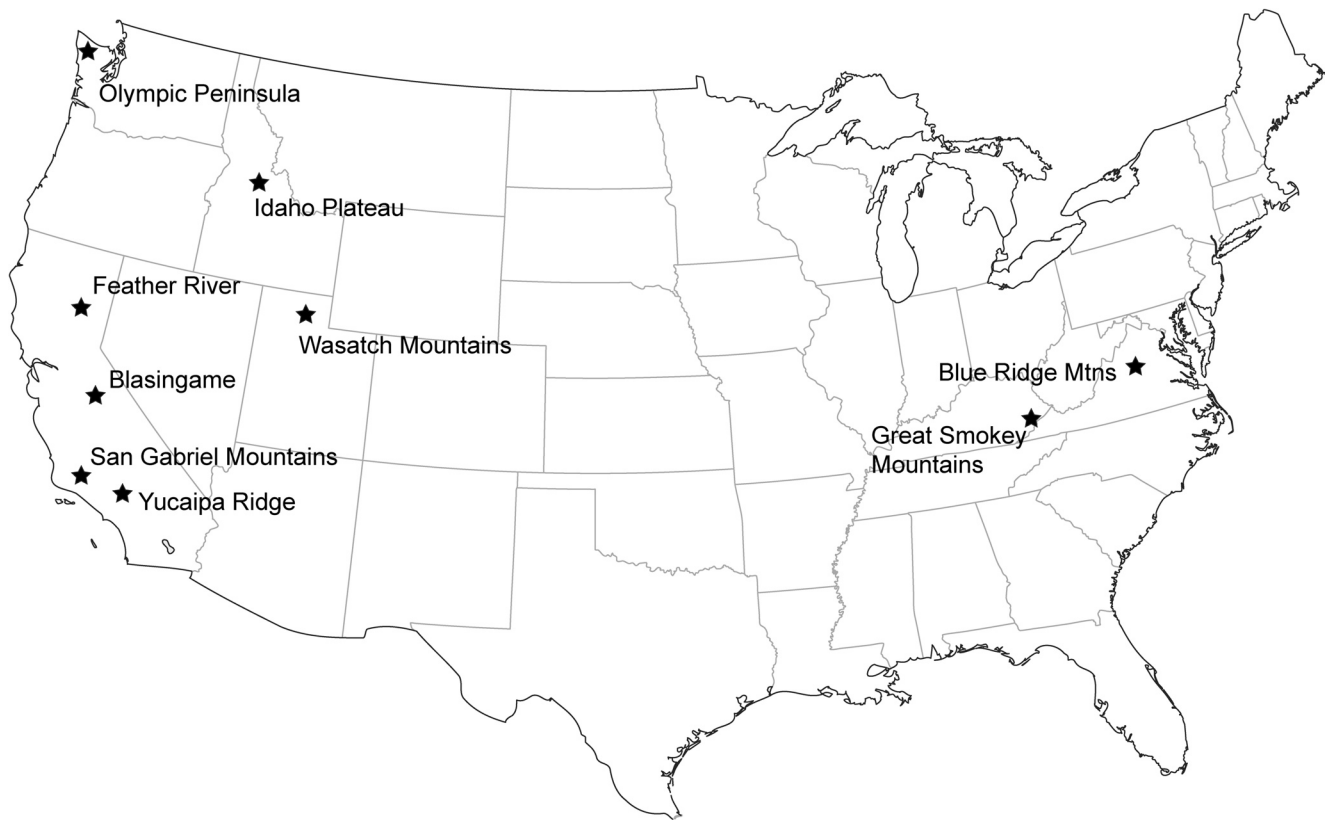


Figure 1. Map of the United States showing the locations of the study sites.

2.2. Erosion Rate Calculations

To ensure a consistent method for calculating erosion rates, they were determined from ^{10}Be concentrations in detrital quartz grains (Table 1). For five of the study regions, published ^{10}Be concentrations were used to calculate basin-scale erosion rates. For the Idaho Plateau sites, ^{10}Be concentrations were measured from soil and fluvial sediment samples collected for this study (see below). For all six study regions, erosion rates were calculated from the ^{10}Be concentrations using a single algorithm (Mudd et al., 2016).

A full description of the Idaho Plateau field area can be found in Wood (2013). Ridgetop and basin-scale denudation rates were determined by measuring cosmogenic ^{10}Be concentrations in quartz (Brown et al., 1995; Granger et al., 1996). The ridgetop rates were determined from soil samples taken from the top 20 cm of the regolith at three sites. For the basin-scale erosion rates, fluvial sediment was taken from three 1st-order streams. Pure quartz fractions from the crushed and sieved (250–710 μm) and magnetically separated samples were obtained using published procedures (Kohl & Nishiizumi, 1992; Mifsud et al., 2013). ICP-OES analysis of purity was undertaken on splits of the etched quartz. Samples were spiked with $\sim 200 \mu\text{g}$ of a commercial Be carrier (Scharlab Beryllium ICP standard solution) and prepared as AMS targets at the University of Cologne using a standard sample preparation method (Binnie et al., 2015). The samples were prepared alongside a reagent blank; ^{10}Be concentrations following blank subtraction are reported in Table 2. Blank corrections are $<2\%$, except for sample S2, for which the correction is $<5\%$. Samples were measured on CologneAMS (Dewald et al., 2013) and normalized to reference standards (Nishiizumi et al., 2007). Uncertainties in the concentrations are estimated by propagating the uncertainties of the AMS measurements and mass of Be added during spiking (estimated 1σ uncertainty of 1%) of both the samples and the blank.

^{10}Be concentrations were converted to denudation rates with the CAIRN software package, which accounts for topographic shielding and snow shielding (Mudd et al., 2016). We calculated snow shielding by first fitting a bilinear trend in snow water equivalent (SWE) as a function of elevation based on regional climate data from the National Oceanic and Atmospheric Association (NOAA, 2016) and following Kirchner

Table 1

Site Information (Na = Not available)

Region	Source	Sample ID	Latitude (°N)	Longitude (°W)	Lithology ^j	MAT ^k (°C)	MAP ^k (cm/yr)	Eros. $\pm 1\sigma$ (mm/kyr)	Med. Crv. ^l (1/m)	Ave. Slope (m/m)	D ^l $\pm 1\sigma$ (cm ² /yr)
San Gabriel Mountains (CA)	a	SG128	34.3376	118.0104	gr	12	55.5	37 \pm 8	−0.02544	0.031	29 \pm 6
	a	SG130	34.3783	117.9893	gr	11	59.8	62 \pm 13	−0.02515	0.028	49 \pm 12
	a	SG131	34.3666	117.9920	gr	11	58.8	85 \pm 20	−0.03410	0.038	50 \pm 10
	a	SG132	34.3658	117.9891	gr	11	60.1	93 \pm 19	−0.04039	0.043	46 \pm 9
	b	na	34.3640	117.9920	gr	na	77.1	108 \pm 17	−0.03086	na	70 \pm 12
Idaho Plateau (ID)	c	S1	45.4773	114.9618	tnlt	8	62.4	55 \pm 11	−0.03254	0.039	34 \pm 7
	c	S2	45.5008	114.9519	tnlt	5	71.0	101 \pm 21	−0.07189	0.025	28 \pm 7
	c	S3	45.5262	114.9293	tnlt	3	116.6	37 \pm 7	−0.02139	0.012	35 \pm 7
	c	R2	45.4843	114.9558	tnlt	7	61.8	78 \pm 16	−0.03083	0.073	51 \pm 11
	c	R3	45.5348	114.9015	tnlt	2	119.8	35 \pm 7	−0.00971	0.019	72 \pm 14
Yucaipa Ridge (CA)	d	3	34.0497	116.9280	qm,gns	9	70.1	922 \pm 203	−0.08083	0.092	228 \pm 57
	d	4	34.0530	116.9401	qm,gns	9	70.1	801 \pm 175	−0.18688	0.159	86 \pm 28
Blasingame (CA)	b	na	36.9540	119.6310	tnlt	na	38.7	30 \pm 4	−0.02727	na	22 \pm 3
Olympic Peninsula (WA)	e	U-WC-S	47.7399	124.0457	gw	8	315.1	177 \pm 39	−0.04884	0.049	72 \pm 17
	e	L-WC-S	47.7302	124.0379	gw	8	315.1	225 \pm 51	−0.04755	0.050	95 \pm 22
	e	L-EFMC-S	47.6581	124.2432	gw	9	319.6	144 \pm 34	−0.04422	0.049	65 \pm 16
Blue Ridge Mountains (VA)	f	SH-01a	38.5713	78.2873	gr	11	107.5	23 \pm 5	−0.01391	0.019	33 \pm 7
	f	SH-02a	38.6636	78.3550	mb	10	104.5	6 \pm 1	−0.00616	0.009	19 \pm 4
	f	SH-07	38.5816	78.4144	gr	10	108.6	10 \pm 2	−0.01699	0.025	12 \pm 2
	f	SH-10	38.6572	78.2822	gr	11	106.8	13 \pm 3	−0.01203	0.018	21 \pm 5
Feather River (CA)	g	BRB-2	39.6491	121.3020	qd	12	140.0	33 \pm 7	−0.02036	0.022	32 \pm 7
	h	BEAN-1	39.6126	121.3295	qd	13	133.2	35 \pm 8	−0.02013	0.024	35 \pm 7
	h	BEAN-2	39.6225	121.3283	qd	14	124.0	38 \pm 8	−0.01969	0.024	39 \pm 8
	h	BEAN-4	39.6237	121.3273	qd	12	136.1	53 \pm 12	−0.02097	0.025	51 \pm 11
	h	BEAN-5	39.6312	121.3298	qd	13	136.5	40 \pm 8	−0.01954	0.024	40 \pm 8
	i	BEAN-7	39.6284	121.3277	qd	13	134.7	85 \pm 18	−0.02557	0.030	67 \pm 14
	i	FT-3	39.6714	121.3109	qd	11	124.8	21 \pm 4	−0.01425	0.017	29 \pm 6
	i	FT-4	39.6712	121.3109	qd	11	123.7	21 \pm 4	−0.01513	0.020	27 \pm 6
	i	FT-6	39.6784	121.3155	qd	10	119.8	19 \pm 4	−0.01338	0.017	29 \pm 6
	i	SB-1	39.7189	121.2411	qd	8	121.9	58 \pm 12	−0.01475	0.019	79 \pm 17
	i	FR-4	39.6344	121.2771	qd	15	140.5	234 \pm 79	−0.04535	0.035	103 \pm 36
	i	FR-5	39.6354	121.2713	qd	15	140.5	124 \pm 39	−0.03858	0.047	64 \pm 21
Wasatch Mtns (Utah)	b	na	40.8920	111.8650	gr	na	51.5	89 \pm 9	−0.02507	na	71 \pm 15
Great Smokey Mtns (NC)	b	na	35.6220	83.2040	qtz	na	154.0	27 \pm 2	−0.02872	na	19 \pm 1

^aSource for ¹⁰Be data and lithology (DiBiase et al., 2010). ^bSource for all data (Richardson et al., 2019). ^cSamples were collected for this study; source for lithology (Wood, 2013). ^dSource for ¹⁰Be data and lithology (Binnie et al., 2015). ^eSource for ¹⁰Be data and lithology (Belmont et al., 2007). ^fSource for ¹⁰Be data and lithology (Duxbury, 2009). ^gSource for ¹⁰Be data for all Feather River samples except FR-4 and FR-5 (Hurst et al., 2012). ^hSource for ¹⁰Be data for FR-4 and FR-5 (Riebe et al., 2001). ⁱSource for lithology (Saucedo & Wagner, 1992). ^jgr = granitic, tnlt = tonalite, qm = quartz monzonite, gns = gneiss, gw = greywacke, mb = metabasalt, qd = quartz diorite, qtz = quartzite. ^kapplies to data from all sources except Richardson et al. (2019); MAT = mean annual temperature; MAP = mean annual precipitation; data from the PRISM Climate Group, <http://prism.oregonstate.edu>, accessed March 25, 2017. ^lValues corrected for grid-resolution effects. Grid-resolution adjustment for sites L-WC-S, L-EFMC-S, SH-01a, SH-02a used a 12-m analysis window because adjustments using 14-window failed to converge to a solution. Sensitivity analyses indicate an average difference of <2% for curvature corrections using a window diameter of 12 versus 14 m.

Table 2
Details of ^{10}Be analysis From Idaho Site

Sample ID	Sample depth intervals (cm)	AMS measurement ID	^{10}Be concentration ($\times 10^3$ at g^{-1})	^{10}Be concentration uncertainty 1σ ($\times 10^3$ at g^{-1})
S1	0–2	s04446	119.9	5.7
S2	8–10	s04447	91.94	7.18
S3	16–18	s04448	373.7	17.8
R2	n/a	s04450	91.49	4.43
R3	n/a	s04451	408.8	15.1
R4	n/a	s04452	480.1	16.6

et al. (2014). SWE averages were converted to snow shielding values by assuming that snow reduces production solely by spallation (Mudd et al., 2016). Snow shielding is highly uncertain because of the difficulty of estimating the average SWE over the timescales of 10^3 – 10^4 years. We calculated denudation rates with no snow shielding to assess the sensitivity of denudation rate to snow thickness and found that, without accounting for snow, denudation rate estimates could be as much as 15% higher (for sample S3) but for most samples, the differences were less than 10%. Uncertainties from analytical error and from uncertainties in production scaling and shielding are presented in Table 1 (Mudd et al., 2016).

2.3. Transport Coefficient Calculations

Direct estimates of the transport efficiency by field measurements of sediment fluxes over relevant time and spatial scales across a range of landscapes are impractical. Instead, along ridgelines, where slopes are

gentle and soil creep is well described by Equation 1, the transport coefficient can be calculated by rewriting Equation 2 as

$$D = - \left(\frac{E}{C_{HT}} \right) \left(\frac{\rho_r}{\rho_s} \right) \quad (3)$$

The ratio ρ_r/ρ_s was assumed to be 2 (Hurst et al., 2012); this value is probably only approximately correct for each of our sites and likely varies by $\pm 25\%$. Ridgeline curvatures were calculated from a 1-m LiDAR DEM for each site using a six-term polynomial function to fit the elevation data within a circular sliding window with a diameter of 14 m. A value of 14 m for the analysis window was chosen based on sensitivity analyses presented by Grieve et al. (2016) who followed the method for identifying the optimal window diameter described by Hurst et al. (2012) and Roering et al. (2010).

The second derivative of the polynomial function at the window's center is that of the cell's two-dimensional curvature. Because topographic noise could produce outliers, the median of the curvatures along each watershed's ridgeline was used in our analyses (Hurst et al., 2012). The average slopes ($\pm 1\sigma$) along the ridgelines, determined as the first derivative of the polynomial function, ranged from $0.5 \pm 3^\circ$ (Blue Ridge Mountains) to $9 \pm 6^\circ$ (Yucaipa Ridge), thereby validating the use of Equation 1. Note that, even at the steepest site along Yucaipa Ridge, nearly 95% of the area analyzed had slopes $< 20^\circ$. Finally, an automated procedure was used to detect the presence of bedrock outcrops along the ridgelines (Milodowski et al., 2015) to confirm that the sites were mantled with soil. One Yucaipa Ridge site had 75% soil cover and the other had 90% soil cover; the soil cover at the other sites ranged from 97% to 100%. Observations of Google EarthTM imagery supported these estimates.

2.4. Additional Data

The data set described above was supplemented with data selected from a compilation presented by Richardson et al. (2019) (Table 1). From this compilation, four sites met our criteria: the ridgelines were symmetrical, transport coefficients were estimated by analyzing ridgetop curvatures from 1-m LiDAR data, erosion rates were determined with cosmogenic ^{10}Be , and the soils were derived from resistant lithologies (Figure 1). The only difference is that Richardson et al. used a 15-m window for their curvature analysis whereas our study used a 14-m window. We consider this difference to be insignificant. With the combined data sets, the sites represent a range of erosion rates from 6 to 922 mm/kyr, a range of mean annual precipitation from 39 to 320 cm/yr, a range of MAT from 2° to 15°C , and a range of aridity index from 0.08 to 1.38 (Table 1).

2.5. Correcting for Grid Resolution

As erosion rates increase, ridgelines become sharper, which could potentially weaken the ability to accurately measure curvature given a fixed grid resolution. In particular, this grid-resolution effect could lead

to an increasing underestimation of curvature as ridgelines sharpen with increasing erosion rates, thereby artificially introducing a positive relationship between D and E . To correct this potential artifact, we performed an analysis in which we compared the estimates of the transport efficiency with those from idealized one-dimensional (1D) hillslopes. We assumed our ridges can be approximated as 1D because the curvature perpendicular to ridgelines far exceeds the curvature parallel to ridgelines.

To begin, we solved for the elevation of an idealized 1D hillslope by assuming that a nonlinear sediment flux law describes sediment transport on our hillslopes (e.g., Andrews & Bucknam, 1987; Roering et al., 1999)

$$q_s = -\frac{D \frac{\partial z}{\partial x}}{1 - \left(\left| \frac{\partial z}{\partial x} \right| / S_c \right)^2} \quad (4)$$

where z is the surface elevation, x is a horizontal distance, and S_c is a critical slope angle. As noted earlier, this equation reduces to Equation 1 at gentle slopes. Inserting Equation 4 into a statement of mass conservation and solving it under steady state conditions yields an expression for the elevation of a hillslope (Roering, Kirchner, & Dietrich, 2001):

$$z = -\frac{S_c^2}{2\beta} \left[\sqrt{D^2 + \left(\frac{2\beta x}{S_c^2} \right)^2} - D \ln \left(\frac{S_c}{2\beta} \sqrt{D^2 + \left(\frac{2\beta x}{S_c^2} \right)^2} + \frac{S_c D}{2\beta} \right) \right] + c \quad (5)$$

where β is the ratio between rock and soil density multiplied by the erosion rate ($(\rho_r/\rho_s)*E$) and c is a constant that sets the absolute elevation of the hillslope profile. At the divide ($x = 0$), the curvature is equal to

$$\left(\frac{d^2 z}{dx^2} \right)_{HT} = -\frac{\beta}{D} \quad (6)$$

As described earlier, the curvature at each site was measured from gridded 1-m topographic data. To mimic this procedure on the synthetic hillslope, we solved Equation 5 on a grid of points with a spacing of 1 m. Random noise was then imposed on each gridded data point from a uniform distribution ranging from -0.1 to 0.1 m, which is a conservative estimate of vertical error in typical airborne LiDAR data. As with the real landscapes, a 2nd-order polynomial equation was fitted across the ridgetop over a 14-m window and the curvature was calculated at the center node.

However, in any gridded topography, the highest true elevation of the ridge may not be located exactly on the grid sampling point. The exact location of the ridge may be offset from the highest gridded pixel by up to half a pixel width. In Equation 5, the ridge is located at $x = 0$ meters, but to account for the possibility that the ridgeline does not correspond to the highest pixel, we allowed the gridded points to shift laterally by 0.5 m to produce an offset between the center point in the gridded data and the ridgeline.

For each study site (Table 1), the values of β and S_c were calculated using the erosion rate and measured curvature to produce idealized ridgetop profiles. Random noise was then applied to the profile, the grid was shifted, and the “synthetic” curvature was calculated from the fitted 2nd-order polynomial. This process was repeated with variations in D until the synthetic curvature matched the curvature measured from the topographic data. We performed 250 iterations of adding random noise to a profile centered on the hilltop, and 250 iterations of random noise to a profile centered 0.5 m from the hilltop. These calculations resulted in 500 values for the sediment transport coefficient that account for (1) sampling a continuous hillslope with gridded data, (2) random noise from the DEM, and (3) a potential mismatch between the actual location of the hillcrest and the highest pixel along the 1D ridge in the DEM.

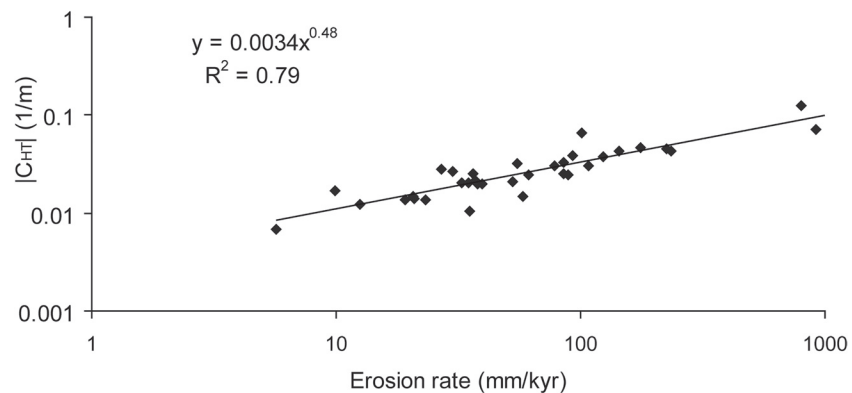


Figure 2. Median hilltop curvature increases with the approximate square root of erosion rate. Because ridgetops have negative curvature, the absolute value of curvature is plotted to allow a power-law regression. For clarity, error bars are not shown here; uncertainties are presented in Table 1.

3. Results

We find that the “raw” hilltop curvature (i.e., uncorrected for grid-scale effects) strongly correlates with the approximate square root of erosion rate: $C_{HT} \propto E^{0.48}$ (Figure 2). The “corrected” hilltop curvature also correlates with erosion rate although the exponent in the regression increases to 0.53 (Figure 3). In addition, the transport coefficient (calculated from the corrected hilltop curvatures) varies with the erosion rate, whereby $D \propto E^{0.47}$ (Figure 4).

The transport efficiency does not correlate with any of the climate parameters (Figure 5) nor with the “effective energy and mass transfer” variable (plot not shown), a parameter which incorporates both MAT and MAP to represent the influence of climate on soil processes (Rasmussen & Tabor, 2007).

4. Discussion

Our results indicate that at the sites we examined, erosion rate appears to have a dominant control on the efficiency of sediment transport. The apparent role of erosion rate on the efficiency of hillslope sediment transport and the insignificance of climate is unexpected considering that others have found a climatic influence on the value of D (Hurst et al., 2013; Richardson et al., 2019). In contrast to our results, Richardson et al. (2019) compiled erosion rate and transport coefficient data from studies which used a variety of techniques to estimate these values, and their data included sites in a range of lithologies as well as from regions with a greater range of precipitation. As a result, their larger data set may be better suited for detecting an underlying climatic influence.

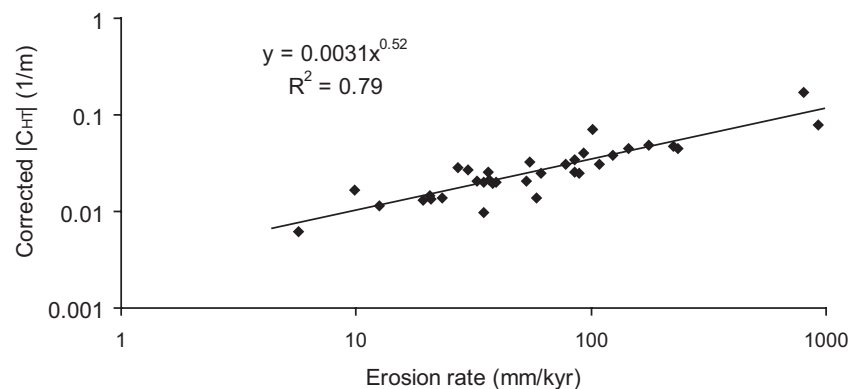


Figure 3. Corrected median hilltop curvature versus erosion rate. Accounting for grid-resolution effects modifies the relationship between curvature and erosion rate, albeit only slightly (compare with Figure 2).

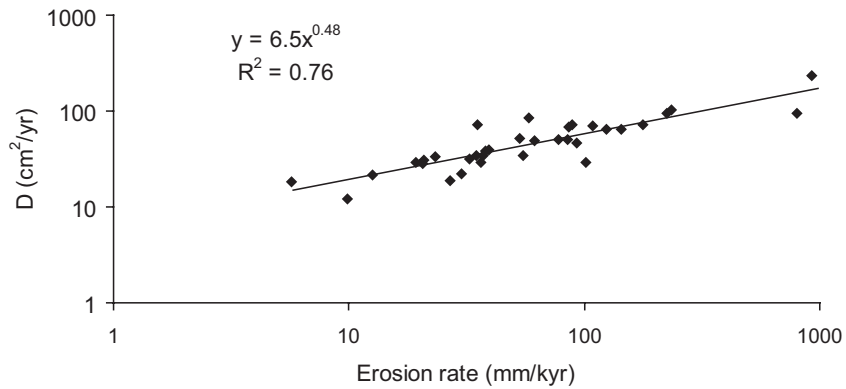


Figure 4. Inferred transport efficiency (D) increases approximately with the square root of erosion rate. D was calculated using the corrected hilltop curvatures.

To explore how transport efficiency might increase with erosion rate, the factors contributing to soil creep can be assessed with two approaches. For discrete, intermittent, large-scale soil creep events (e.g., tree throw), the transport efficiency can be calculated as

$$D = f_e \bar{V} \bar{d} \quad (7)$$

where f_e is the frequency of events per unit area ($T^{-1} L^{-2}$), \bar{V} is the average volume (L^3) of soil displaced with each event, and \bar{d} is the average distance (L) that the volume of soil is displaced (Gabet, 2000). For example, in the case of tree throw, the transport coefficient will depend on the number of toppled trees over a period of time, the average volume of soil in the root plates, and the distance that the root plates are displaced (Gabet et al., 2003). We are not aware of any reason why any of these three factors would increase with erosion rate. Indeed, in the case of bioturbation, \bar{V} and f_e might be expected to decrease. For instance, because soils tend to be thinner where erosion rates are high (e.g., Gabet et al., 2015), the volume of soil available for transport by tree throw should decrease. In addition, the frequency of bioturbation might be expected to decrease in rapidly eroding landscapes because of lower plant biomass (Milodowski et al., 2014).

For dilational creep processes in which soil particles are lofted up and then settle down due to gravity, D can be expressed as (Furbish et al., 2009)

$$D = k R h N_a \left(1 - \frac{P}{P_m} \right)^2 \cos^2 \theta \quad (8)$$

where k is an empirically determined dimensionless constant that accounts for particle shape and the relationship between mean free path length and the vertical displacement of particles, R is particle radius (L), h is soil thickness (L), P is the particle concentration ($L^3 L^{-3}$), P_m is the maximum value of P , N_a is the particle activation rate (T^{-1}), θ is the hillslope angle ($^\circ$ equal to zero at the ridge crest), and the overbar signifies vertically averaged quantities. Particle concentration (a function of soil bulk density) is not likely to be dependent on the erosion rate to a significant degree and if it is, the term in parentheses would likely decrease with increasing erosion rate, thereby suppressing the value of D . Because soils are thinner in rapidly eroding landscapes (e.g., Gabet et al., 2015), variations in soil thickness also cannot account for the increase in transport efficiency with erosion rate; indeed, the inverse relationship between soil thickness and erosion rate should lead to an inverse relationship between D and E , the opposite of what we have found. With respect to particle activation rate, we are not aware of any studies that have correlated this variable with erosion rate; however, because rapidly eroding hillslopes tend to have thinner and more exposed soils (e.g., Gabet et al., 2015), the particle activation rate in these landscapes could potentially be higher, which could lead to an increase in D with E . For example, a decrease in vegetation biomass with increasing erosion rate (Milodowski et al., 2014) could leave the soil surface more vulnerable to raindrop impact (Dunne et al., 2010). Nevertheless, as noted above, a reduction in biomass might also be expected to damp bioturbation, thereby reducing transport efficiency.

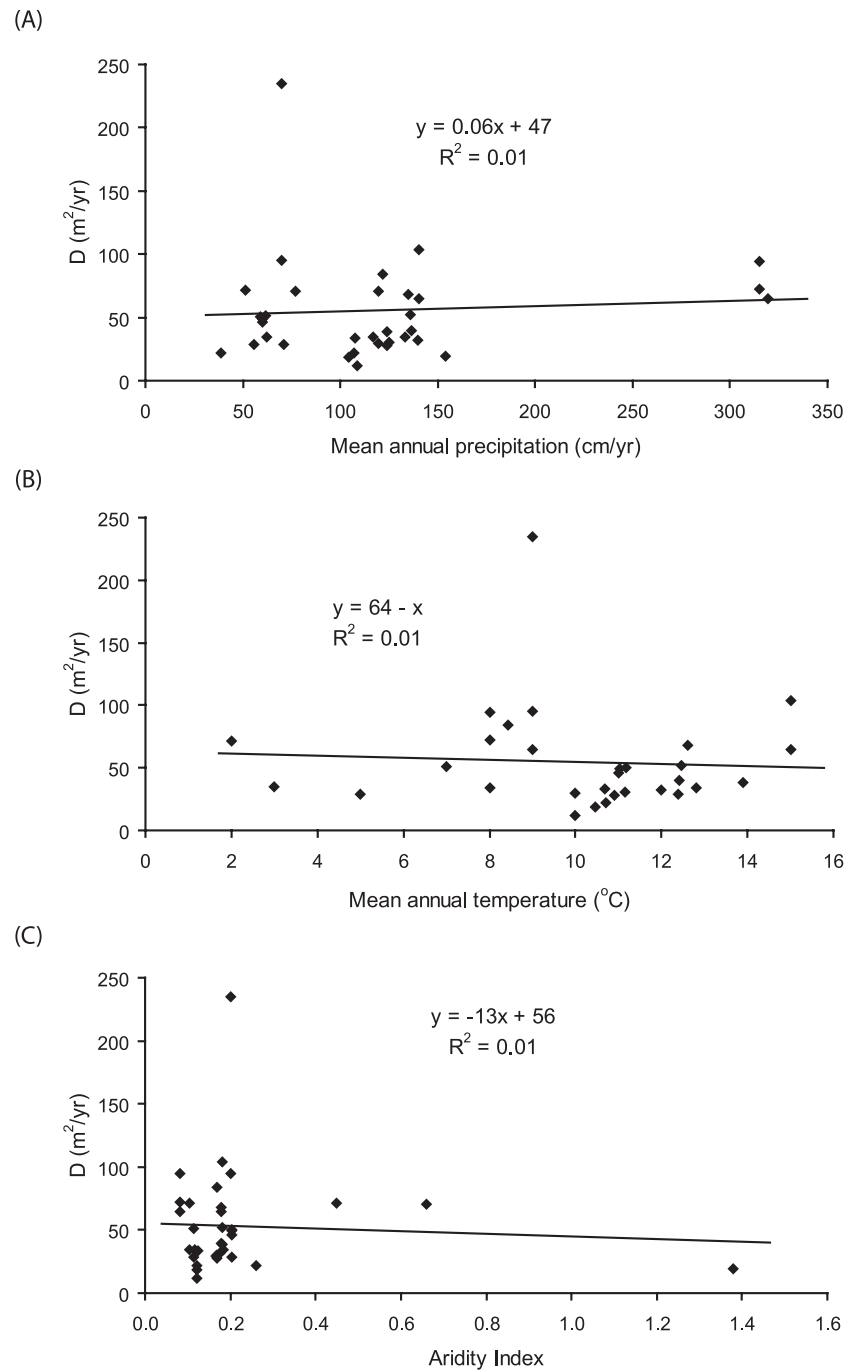


Figure 5. Inferred transport efficiency (D) versus various climatic measures. Inferred transport efficiency does not depend on mean annual precipitation (a), mean annual temperature (b), or the aridity index (c). Note that the plot for mean annual temperature does not include the data set from Richardson et al. (2019), which did not provide these values.

The final variable from Equation 8 to be explored is the particle diameter, R . Previous studies have documented an increase in particle diameter with erosion rate (Attal et al., 2015; Riebe et al., 2015). Where erosion is slow, particles are exposed to weathering processes for longer periods of time because of longer soil residence times and as a result, particles become smaller (e.g., Mudd & Yoo, 2010). In Equation 8, particle size is a factor in the transport coefficient because it controls the mean free path of particles in a soil creeping by dilational processes (Furbish et al., 2009). Although field data from Neely et al. (2019) suggest

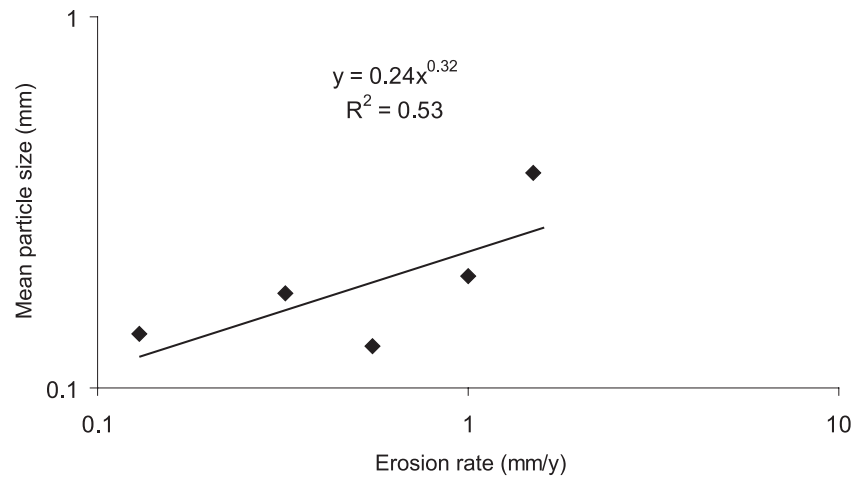


Figure 6. Geometric mean of particle size (R) increases with inferred erosion rate (E) at the Feather River site (Gabet et al., 2015). Particle sizes of soil surface samples were measured at regular intervals along a ridge with a gradient in erosion rates. Because local topography along the ridgeline (i.e., saddles and knobs) was found to have a strong control on soil properties at this site, we present here only the data from the knobs. Erosion rate calculated from ridgetop curvatures using the relationship reported in the present study. 1σ for particle size data averages 5.8 mm (error bars not shown for clarity).

that coarser soils have a lower transport coefficient, laboratory experiments have demonstrated that, for the same input of energy, coarse-grained soils will creep faster than fine-grained soils (Supporting information to Deshpande et al., 2020). In addition, of the various factors that could affect the rate of soil creep, particle size is the one with the most potential to vary by multiple orders-of-magnitude between watersheds eroding at different rates (Marshall & Sklar, 2012). For example, while the data are limited, particle radius along a ridgeline increases with the erosion rate at the Feather River site (Figure 6).

While particle size is a potential candidate for explaining the relationship between the transport efficiency and erosion rate found here, this hypothesis raises some perplexing issues. First, whereas the relationship between particle size and erosion rate is likely to be constant within a single region, one would expect it to vary between regions according to climate and lithology (although we tried to control for rock strength, variations in texture, for example, could affect particle size). However, despite the expected regional variations in these factors, the sites fall along the same D versus E trend line (Figure 3). Second, because the more rapid weathering rates in wetter climates should lead to smaller soil particles (Marshall & Sklar, 2012), the transport coefficient should decrease in wetter climates. However, we find no relationship between mean annual precipitation and D (Figure 5).

Another potential explanation may be that transport efficiency is sensitive to slope. Landscapes that are eroding quickly are generally steeper than those that are eroding more slowly. For example, the slopes at the ridge crests (S_{HT}) at our sites increase with the approximate square root of erosion rate (Figure 7). Some properties of the soil (e.g., its resistance to disturbance) may be affected by the gradient such that its transport efficiency increases on steeper slopes (P. Richardson, pers. comm). Furbish and Haff (2010) suggest that the rate at which soil is mobilized might also increase with slope. To explore the consequences of a slope-dependent transport coefficient, we define a new variable, D_s (L^2/T)

$$D_s = KS \quad (10)$$

such that

$$q_s = D_s S \quad (11a)$$

or

$$q_s = KS^2 \quad (11b)$$

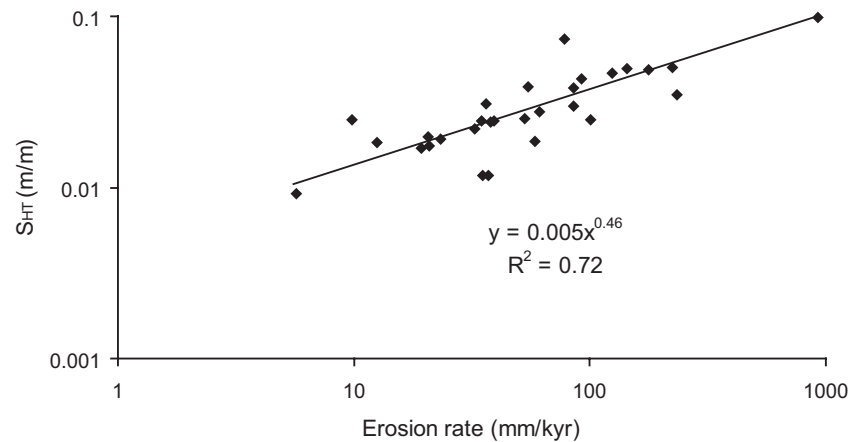


Figure 7. Mean slope at the ridgeline increases with erosion rate. The steeper slopes generally found in rapidly eroding landscapes can also be recognized along the ridge crests.

where $K (L^2/T)$ is a constant with the same properties as D . Inserting Equation 11b into a statement of mass conservation

$$\rho_r \frac{dz}{dt} = -\rho_s \frac{dq_s}{dx} \quad (12)$$

and integrating twice assuming steady state ($dz/dt = E$) and $\rho_r/\rho_s = 2$ yields

$$E = KCS / 2 \quad (13a)$$

To specify that this relationship is applied to the hilltops, we rewrite it as

$$E = KC_{HT}S_{HT} / 2 \quad (13b)$$

Thus, the assumption that the transport coefficient increases linearly with slope implies a linear relationship between the erosion rate and the product of curvature and slope. Indeed, a power-law regression between the two yields an exponent of unity for our data, offering support for the hypothesis that the transport coefficient is slope-dependent (Figure 8). However, because slope and curvature are linearly related along a parabolic curve, Equation 13b is functionally equivalent to $E \propto C^2$ or $C \propto E^{1/2}$, which is the original relationship presented in Figure 3. In other words, the linear relationship between E and the product of C_{HT} and S_{HT} may simply be a mathematical artifact, and the sediment flux relationship represented by Equation 11b would need to be validated independently. Finally, note that Equation 11b is quite different from the nonlinear sediment flux equation proposed elsewhere (Andrews & Bucknam, 1987; Gabet, 2003; Roering et al., 1999), particularly at lower slopes (Figure 9).

The lack of a clear and robust mechanistic link between D and E , as well as the square root dependency of the hilltop curvature on erosion rate when Equation 2 predicts a linear relationship, suggests that the present theory explaining the profile of soil-mantled hillslopes is incomplete. We tentatively propose that, in resistant lithologies, hillslope curvature may be partially, if not mostly, controlled by processes occurring within the bedrock, rather than the soil. Indeed, in an eroding landscape, the soil on a hill is just a thin mantle covering a much larger bedrock mass; the shape of the hill, therefore, should reflect the shape of the underlying bedrock and the processes acting within it (e.g., Rempe & Dietrich, 2014). However, the absence of any climatic influence in our results suggests that these bedrock processes are not associated with the typical chemical and physical weathering processes; instead, they are likely related to a more universal mechanism. Recent work has begun investigating how, even in soil-mantled landscapes, the generation of fractures in bedrock by topographic stresses may exert an important influence on landform shape (e.g., Clair et al., 2015; Pelletier, 2017; Slim et al., 2015). However, whereas the regional tectonic stress is an important contributor to topographic stresses (e.g., Clair et al., 2015; Miller & Dunne, 1996), the tectonic stress

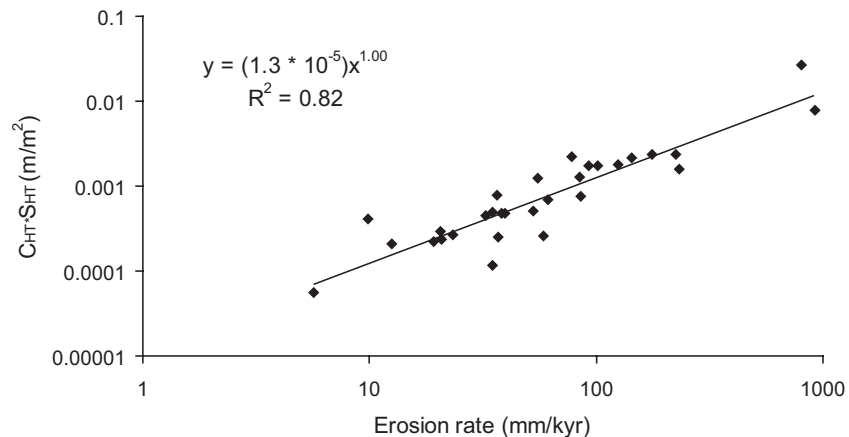


Figure 8. Product of hilltop curvature and slope versus erosion rate. The nearly linear relationship between the two supports a sediment flux law of the form $q_s = KS^2$; however, this linear relationship may be a mathematical artifact.

regime varies widely between our sites. For example, the regional stresses are compressional in the San Gabriel Mountains but extensional in the Wasatch Mountains and the Feather River study area (Heidbach et al., 2016; Wakabayashi & Sawyer, 2000). Therefore, the alignment of these sites along the same trend line (Figure 2) suggests that our present understanding of rock fracture by topographic stresses is unable to explain our results.

One potential avenue for further investigations may be an examination of the time-dependent nature of fracture growth. At high erosion rates, near-surface bedrock is rejuvenated more quickly, thereby limiting the fracture density. In contrast, in environments where the erosion rate is slower and the rejuvenation of the surface occurs less frequently, the near-surface bedrock may have a higher fracture density as it accumulates damage over time. The relationship found here between hilltop curvature and erosion rate, therefore, may be related to the strength of the underlying rock mass in a way that is not yet understood. As a preliminary test of this idea, we analyzed the data from four sites that met our criteria but were underlain by presumably weak lithologies, sedimentary bedrock, or highly sheared metamorphic bedrock (Perron et al., 2012;

Richardson et al., 2019). A comparison of the hilltop curvatures between our original data set consisting of resistant rocks and the data from the weaker lithologies suggests that, for the same erosion rate, the weaker bedrock forms hilltops with lower curvatures (Figure 10). While the data set from presumably weak lithologies is limited, it supports our hypothesis that a weaker bedrock is associated with lower curvatures. Although one might argue that the lower curvatures seen in hillslopes underlain by weaker lithologies could be a result of higher transport efficiencies, a clear mechanistic link between bedrock strength and transport efficiency is lacking, especially considering that many soil creep processes (e.g., tree throw) do not appear to be limited by soil texture.

If bedrock processes have an important influence on hillslope form, then hilltop curvature cannot be used for estimating the transport coefficient, at least in landscapes underlain by resistant rock. This limitation might explain why we were unable to detect any climatic influence on D , in contrast to compilations that include estimates of D from a variety of techniques (Hurst et al., 2013; Richardson et al., 2019). In addition, if hillslope form is primarily dependent on the underlying bedrock, estimates of D based on topographic characteristics might be expected to be of different magnitudes than estimates from other techniques. Indeed, in the compilation presented by Richardson et al. (2019), transport coefficients estimated from relief and hilltop curvature are generally 5–10

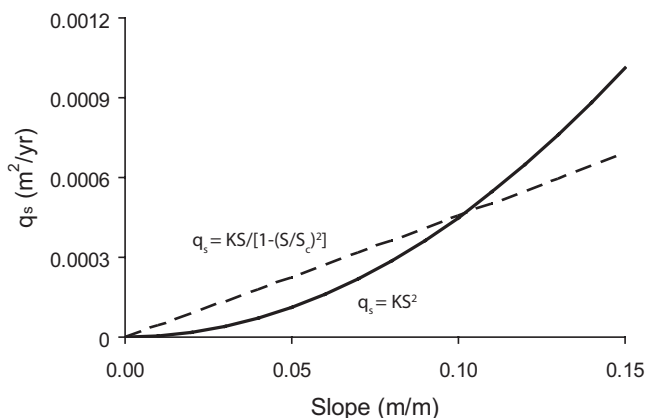


Figure 9. Comparison of nonlinear sediment flux equations. Dashed line represents the commonly used nonlinear equation calibrated with values determined in Roering et al. (1999). Solid line represents fluxes calculated with Equation 11b and calibrated to provide a comparison with the dashed line. Fluxes were calculated over the range of hilltop gradients measured at our field sites. Note that a linear regression (not shown) through the dashed line yields an R^2 of 0.9999, confirming the use of Equation 1 as an appropriate substitute for the standard nonlinear equation at low slopes.

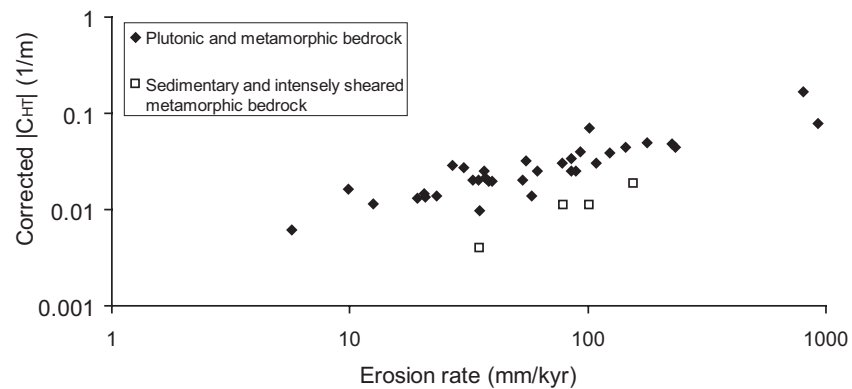


Figure 10. Curvature versus erosion rate according to rock type. For the same erosion rate, the hilltop curvature is lower at sites underlain with presumably weaker bedrock when compared to sites with stronger bedrock. Sites shown with the square markers are Tennessee Valley (CA), Oregon Coast Range (OR), Gabilan Mesa (CA), and Allegheny Plateau (PA; Perron et al., 2012; Richardson et al., 2019).

times higher than those estimated from the modeling of scarps for the same aridity index (a factor that was determined to be a control on D) despite the fact that estimates based on scarp evolution were often performed on slopes comprised of unconsolidated sediment, which might be expected to have higher values of D . Therefore, the mismatch between the estimates of the transport coefficient based on topographic metrics and those based on other techniques suggests that some other factor is influencing hillslope shape.

5. Conclusions

The square-root dependency of hilltop curvature on the erosion rate challenges the prevailing theory linking soil creep to the shape of soil-mantled hillslopes, which predicts a linear relationship between the two. This dependency could be explained if the transport coefficient also varies with the square root of erosion rate. However, we are unable to propose a robust mechanism linking transport coefficient to the erosion rate. Given the difficulties in accounting for our results within the standard theory of hillslope evolution, we tentatively propose that in landscapes underlain by resistant lithologies, hillslope curvature is not primarily related to soil creep but is, instead, controlled by processes in the underlying bedrock.

Finally, the robust relationship between ridgetop curvature and erosion rate across a range of climatic conditions suggests that the latter can be estimated directly from topographic analysis in rock types similar to those analyzed in this study. However, erosion rates determined with this procedure must incorporate uncertainties in the original ^{10}Be erosion rate measurements, uncertainties in the curvature measurements, and the uncertainty in the regression between C_{HT} and E . Nevertheless, our results have the potential for providing a simple approach for estimating watershed-scale erosion rates through the measurement of hilltop curvatures.

Conflict of Interest

The authors declare no conflicts of interest relevant to this study.

Data Availability Statement

Original data for this research study are provided in Tables 1 and 2. Additional data were compiled from Belmont et al. (2007), Binnie et al. (2007), DiBiase et al. (2010), Duxbury (2009), Hurst et al. (2012), Richardson et al. (2019), and Riebe et al. (2001). LiDAR elevation data were acquired with a Seed Project from the National Center for Airborne Laser Mapping in the summer of 2011.

Acknowledgments

Idaho field work for this project was conducted with assistance from B. Wood, S. Powell, and E. Hewitt. The data supporting the conclusions can be found in the tables and references. This project was partially funded by graduate student research grants from GSA and SJSU. The software used for analysis was developed under NERC grant NE/J009970/1. The authors are grateful to J. Pelletier, J. Roering, and P. Richardson for their careful reviews and helpful comments and to D. Furbish for extended and insightful discussions.

References

- Anderson, H. W., Coleman, G. B., & Zinke, P. J. (1959). Summer slides and winter scour, dry-wet erosion in Southern California mountains: U.S.D.A., Forest Service. In *Pacific Southwest Forest and Range Experiment Station Technical Paper PSW-36*, U.S. Forest Service.
- Anderson, R. S., Anderson, S. P., & Tucker, G. E. (2013). Rock damage and regolith transport by frost: An example of climate modulation of the geomorphology of the critical zone. *Earth Surface Processes and Landforms*, 38(3), 299–316. <https://doi.org/10.1002/esp.3330>
- Andrews, D. J., & Bucknam, R. C. (1987). Fitting degradation of shoreline scarps by a nonlinear diffusion model. *Journal of Geophysical Research*, 92(B12), 12857–12867. <https://doi.org/10.1029/jb092ib12p12857>
- Attal, M., Mudd, S. M., Hurst, M. D., Weinman, B., Yoo, K., & Naylor, M. (2015). Impact of change in erosion rate and landscape steepness on hillslope and fluvial sediments grain size in the Feather River Basin (Sierra Nevada, California). *Earth Surface Dynamics*, 2, 1047–1092.
- Belmont, P., Pazzaglia, F. J., & Gosse, J. C. (2007). Cosmogenic ^{10}Be as a tracer for hillslope and channel sediment dynamics in the Clearwater River, western Washington State. *Earth and Planetary Science Letters*, 264, 123–135. <https://doi.org/10.1016/j.epsl.2007.09.013>
- Ben-Asher, M., Haviv, I., Roering, J. J., & Crouvi, O. (2017). The influence of climate and microclimate (aspect) on soil creep efficiency: Cinder cone morphology and evolution along the eastern Mediterranean Golan Heights. *Earth Surface Processes and Landforms*, 42(15), 2649–2662. <https://doi.org/10.1002/esp.4214>
- Binnie, S. A., Dunai, T. J., Voronina, E., Goral, T., Heinze, S., & Dewald, A. (2015). Separation of Be and Al for AMS using single-step column chromatography. *Nuclear Instruments and Methods in Physics Research Section B: Beam Interactions with Materials and Atoms*, 361, 397–401. <https://doi.org/10.1016/j.nimb.2015.03.069>
- Binnie, S. A., Phillips, W. M., Summerfield, M. A., & Fifield, L. K. (2007). Tectonic uplift, threshold hillslopes, and denudation rates in a developing mountain range. *Geology*, 35, 743–746. <https://doi.org/10.1130/g23641a.1>
- Brown, E. T., Stallard, R. F., Larsen, M. C., Raisbeck, G. M., & Yiu, F. (1995). Denudation rates determined from the accumulation of in situ-produced ^{10}Be in the Luquillo Experimental Forest, Puerto Rico. *Earth and Planetary Science Letters*, 129(1–4), 193–202. [https://doi.org/10.1016/0012-821x\(94\)00249-x](https://doi.org/10.1016/0012-821x(94)00249-x)
- Carson, M. A., & Kirkby, M. J. (1972). *Hillslope form and process* (pp. 475). Cambridge University Press.
- Clair, J. S., Moon, S., Holbrook, W. S., Perron, J. T., Riebe, C. S., Martel, S. J., et al. (2015). Geophysical imaging reveals topographic stress control of bedrock weathering. *Science*, 350, 534–538.
- Culling, W. E. H. (1963). Soil creep and the development of hillside slopes. *The Journal of Geology*, 71, 127–161. <https://doi.org/10.1086/626891>
- Denny, C., & Goodlett, J. (1956). Microrelief Resulting from Fallen Trees (Vol. 288, pp. 59–68). USGS Professional Publication.
- Deshpande, N., Furbish, D., Arratia, P., & Jerolmack, D. (2020). The perpetual fragility of creeping hillslopes. *EarthArXiv*. <https://doi.org/10.31223/osf.io/qc9jh>
- Dewald, A., Heinze, S., Jolie, J., Zilges, A., Dunai, T., Rethemeyer, J., et al. (2013). CologneAMS, a dedicated center for accelerator mass spectrometry in Germany. *Nuclear Instruments and Methods in Physics Research Section B: Beam Interactions with Materials and Atoms*, 294, 18–23. <https://doi.org/10.1016/j.nimb.2012.04.030>
- DiBiase, R. A., Whipple, K. X., Heimsath, A. M., & Ouimet, W. B. (2010). Landscape form and millennial erosion rates in the San Gabriel Mountains, CA. *Earth and Planetary Science Letters*, 289, 134–144. <https://doi.org/10.1016/j.epsl.2009.10.036>
- Dunne, T., Malmon, D. V., & Mudd, S. M. (2010). A rain splash transport equation assimilating field and laboratory measurements. *Journal of Geophysical Research*, 115(F1), 1–16.
- Duxbury, J. (2009). *Erosion rates in and around the Shenandoah National Park, VA, determined using analysis of cosmogenic ^{10}Be* , MS thesis (pp. 123). University of Vermont.
- Fernandes, N. F., & Dietrich, W. E. (1997). Hillslope evolution by diffusive processes: the timescale for equilibrium adjustments. *Water Resources Research*, 33(6), 1307–1318. <https://doi.org/10.1029/97wr00534>
- Furbish, D. J., & Haff, P. K. (2010). From divots to swales: Hillslope sediment transport across diverse length scales. *Journal of Geophysical Research*, 115(F3). <https://doi.org/10.1029/2009JF001576>
- Furbish, D. J., Haff, P. K., Dietrich, W. E., & Heimsath, A. M. (2009). Statistical description of slope-dependent soil transport and the diffusion-like coefficient. *Journal of Geophysical Research*, 114(F3). <https://doi.org/10.1029/2009JF001267>
- Gabet, E. J. (2000). Gopher bioturbation: Field evidence for non-linear hillslope diffusion. *Earth Surface Processes and Landforms*, 25(13), 1419–1428. [https://doi.org/10.1002/1096-9837\(200012\)25:13<1419::aid-esp148>3.0.co;2-1](https://doi.org/10.1002/1096-9837(200012)25:13<1419::aid-esp148>3.0.co;2-1)
- Gabet, E. J. (2003). Sediment transport by dry ravel. *Journal of Geophysical Research*, 108(B1), 2050. <https://doi.org/10.1029/2001JB001686>
- Gabet, E. J. (2020). Lithological and structural controls on river profiles and networks in the northern Sierra Nevada. *The Geological Society of America Bulletin*, 132(3–4), 655–667. <https://doi.org/10.1130/b35128.1>
- Gabet, E. J., Mudd, S. M., Milodowski, D. T., Yoo, K., Hurst, M. D., & Dosseto, A. (2015). Local topography and erosion rate control regolith thickness along a ridge line in the Sierra Nevada, California. *Earth Surface Processes and Landforms*, 40(13), 1779–1790. <https://doi.org/10.1002/esp.3754>
- Gabet, E. J., Reichman, O. J., & Seabloom, E. (2003). The effects of bioturbation on soil processes and sediment transport. *Annual Review of Earth and Planetary Sciences*, 31, 259–273. <https://doi.org/10.1146/annurev.earth.31.100901.141314>
- Gilbert, G. K. (1909). The convexity of hilltops. *The Journal of Geology*, 17, 344–350. <https://doi.org/10.1086/621620>
- Granger, D. E., Kirchner, J. W., & Finkel, R. (1996). Spatially averaged long-term erosion rates measured from in situ-produced cosmogenic nuclides in alluvial sediment. *The Journal of Geology*, 104(3), 249–257. <https://doi.org/10.1086/629823>
- Grieve, S. W. D., Mudd, S. M., & Hurst, M. D. (2016). How long is a hillslope? *Earth Surface Processes and Landforms*, 41(8), 1039–1054. <https://doi.org/10.1002/esp.3884>
- Hack, J. T. (1973). Stream-profile analysis and stream-gradient index. *Journal of Research of the U. S. Geological Survey*, 1(4), 421–429.
- Hanks, T. C. (2000). The age of scarplike landforms from diffusion-equation analysis. *Quaternary Geochronology: Methods and Applications*, 313–338.
- Hanks, T. C., & Schwartz, D. P. (1987). Morphologic dating of the pre-1983 fault scarp on the Lost River Fault at Doublespring Pass Road, Custer County, Idaho. *Bulletin of the Seismological Society of America*, 77, 837–846.
- Harel, M.-A., Mudd, S. M., & Attal, M. (2016). Global analysis of the stream power law parameters based on worldwide ^{10}Be denudation rates. *Geomorphology*, 268, 184–196. <https://doi.org/10.1016/j.geomorph.2016.05.035>
- Heidbach, O., Rajabi, M., Reiter, K., Ziegler, M., & Team, W. (2016). *World Stress Map Database Release 2016, v.1.1*. GFZ Data Services.
- Heimsath, A. M., Furbish, D. J., & Dietrich, W. E. (2005). The illusion of diffusion: Field evidence for depth-dependent sediment transport. *Geology*, 33(12), 949–952. <https://doi.org/10.1130/g21868.1>

- Hurst, M. D., Mudd, S. M., Walcott, R. C., Attal, M., & Yoo, K. (2012). Using hilltop curvature to derive the spatial distribution of erosion rates. *Journal of Geophysical Research*, 115, 1–19.
- Hurst, M. D., Mudd, S. M., Yoo, K., Attal, M., & Walcott, R. (2013). Influence of lithology on hillslope morphology and response to tectonic forcing in the northern Sierra Nevada of California. *Journal of Geophysical Research: Earth Surface*, 118, 832–851. <https://doi.org/10.1002/jgrf.20049>
- Kirchner, P. B., Bales, R. C., Molotch, N. P., Flanagan, J., & Guo, Q. (2014). LiDAR measurement of seasonal snow accumulation along an elevation gradient in the southern Sierra Nevada, California. *Hydrology and Earth System Sciences*, 18, 4261–4275. <https://doi.org/10.5194/hess-18-4261-2014>
- Kohl, C. P., & Nishiizumi, K. (1992). Chemical isolation of quartz for measurement of in-situ -produced cosmogenic nuclides. *Geochimica et Cosmochimica Acta*, 56(9), 3583–3587. [https://doi.org/10.1016/0016-7037\(92\)90401-4](https://doi.org/10.1016/0016-7037(92)90401-4)
- Marshall, J. A., & Sklar, L. S. (2012). Mining soil databases for landscape-scale patterns in the abundance and size distribution of hillslope rock fragments. *Earth Surface Processes and Landforms*, 37(3), 287–300. <https://doi.org/10.1002/esp.2241>
- Mifsud, C., Fujioka, T., & Fink, D. (2013). Extraction and purification of quartz in rock using hot phosphoric acid for in situ cosmogenic exposure dating. *Nuclear Instruments and Methods in Physics Research Section B: Beam Interactions with Materials and Atoms*, 294, 203–207. <https://doi.org/10.1016/j.nimb.2012.08.037>
- Miller, D. J., & Dunne, T. (1996). Topographic perturbations of regional stresses and consequent bedrock fracturing. *Journal of Geophysical Research*, 101(B11), 25523–25536.
- Milodowski, D. T., Mudd, S. M., & Mitchard, E. T. (2014). Erosion rates as a potential bottom-up control of forest structural characteristics in the Sierra Nevada Mountains. *Ecology*, 96(1), 31–38.
- Milodowski, D. T., Mudd, S. M., & Mitchard, E. T. A. (2015). Topographic roughness as a signature of the emergence of bedrock in eroding landscapes. *Earth Surface Dynamics*, 3(4), 483–499. <https://doi.org/10.5194/esurf-3-483-2015>
- Mudd, S. M. (2017). Detection of transience in eroding landscapes. *Earth Surface Processes and Landforms*, 42(1), 24–41. <https://doi.org/10.1002/esp.3923>
- Mudd, S. M., Harel, M.-A., Hurst, M. D., Grieve, S. W. D., & Marrero, S. M. (2016). The CAIRN method: Automated, reproducible calculation of catchment-averaged denudation rates from cosmogenic nuclide concentrations. *Earth Surface Dynamics*, 4, 655–674. <https://doi.org/10.5194/esurf-4-655-2016>
- Mudd, S. M., & Yoo, K. (2010). Reservoir theory for studying the geochemical evolution of soils. *Journal of Geophysical Research*, 115(F3). <https://doi.org/10.1029/2009jf001591>
- Neely, A. B., DiBiase, R. A., Corbett, L. B., Bierman, P. R., & Caffee, M. W. (2019). Bedrock fracture density controls on hillslope erodibility in steep, rocky landscapes with patchy soil cover, southern California, USA. *Earth and Planetary Science Letters*, 522, 186–197. <https://doi.org/10.1016/j.epsl.2019.06.011>
- Nishiizumi, K., Imamura, M., Caffee, M. W., Southon, J. R., Finkel, R. C., & McAninch, J. (2007). Absolute calibration of ^{10}Be AMS standards. *Nuclear Instruments and Methods in Physics Research Section B: Beam Interactions with Materials and Atoms*, 258(2), 403–413. <https://doi.org/10.1016/j.nimb.2007.01.297>
- NOAA. (2016). National Center for Environmental Information, edited.
- Pelletier, J. D. (2017). Quantifying the controls on potential soil production rates: a case study of the San Gabriel Mountains, California. *Earth Surface Dynamics*, 5(3), 479–492. <https://doi.org/10.5194/esurf-5-479-2017>
- Pelletier, J. D., McGuire, L. A., Ash, J. L., Engelder, T. M., Hill, L. E., Leroy, K. W., et al. (2011). Calibration and testing of upland hillslope evolution models in a dated landscape: Banco Bonito, New Mexico. *Journal of Geophysical Research*, 116(F4). <https://doi.org/10.1029/2011jf001976>
- Perron, J. T., Richardson, P. W., Ferrier, K. L., & Lapôtre, M. (2012). The root of branching river networks. *Nature*, 492, 100–103. <https://doi.org/10.1038/nature11672>
- PRISM. (2014). PRISM Climate Group, edited.
- Rasmussen, C., & Tabor, N. J. (2007). Applying a quantitative pedogenic energy model across a range of environmental gradients. *Soil Science Society of America Journal*, 71(6), 1719–1729. <https://doi.org/10.2136/sssaj2007.0051>
- Rempe, D. M., & Dietrich, W. E. (2014). A bottom-up control on fresh-bedrock topography under landscapes. *Proceedings of the National Academy of Sciences*, 111(18), 6576–6581. <https://doi.org/10.1073/pnas.1404763111>
- Richardson, P. W., Perron, J. T., & Schurr, N. D. (2019). Influences of climate and life on hillslope sediment transport. *Geology*, 47, 423–426. <https://doi.org/10.1130/g45305.1>
- Riebe, C. S., Kirchner, J. W., Granger, D. E., & Finkel, R. C. (2001). Minimal climatic control on erosion rates in the Sierra Nevada, California. *Geology*, 29(5), 447–450. [https://doi.org/10.1130/0091-7613\(2001\)029<0447:mccoer>2.0.co;2](https://doi.org/10.1130/0091-7613(2001)029<0447:mccoer>2.0.co;2)
- Riebe, C. S., Sklar, L. S., Lukens, C. E., & Shuster, D. L. (2015). Climate and topography control the size and flux of sediment produced on steep mountain slopes. *Proceedings of the National Academy of Sciences of the United States of America*, 112(51), 15574–15579. <https://doi.org/10.1073/pnas.1503567112>
- Roering, J. J., Kirchner, J. W., & Dietrich, W. E. (1999). Evidence for nonlinear, diffusive sediment transport on hillslopes and implications for landscape morphology. *Water Resources Research*, 35(3), 853–870. <https://doi.org/10.1029/1998wr900090>
- Roering, J. J., Kirchner, J. W., & Dietrich, W. E. (2001). Hillslope evolution by nonlinear, slope-dependent transport: Steady state morphology and equilibrium adjustment timescales. *Journal of Geophysical Research*, 106(B8), 16499–16513. <https://doi.org/10.1029/2001jb000323>
- Roering, J. J., Kirchner, J. W., Sklar, L. S., & Dietrich, W. E. (2001). Hillslope evolution by nonlinear creep and landsliding: An experimental study. *Geology*, 29(2), 143–146. [https://doi.org/10.1130/0091-7613\(2001\)029<0143:hebnc>2.0.co;2](https://doi.org/10.1130/0091-7613(2001)029<0143:hebnc>2.0.co;2)
- Roering, J. J., Marshall, J., Booth, A. M., Mort, M., & Jin, Q. (2010). Evidence for biotic controls on topography and soil production. *Earth and Planetary Science Letters*, 298, 183–190. <https://doi.org/10.1016/j.epsl.2010.07.040>
- Roering, J. J., Perron, J. T., & Kirchner, J. W. (2007). Functional relationships between denudation and hillslope form and relief. *Earth and Planetary Science Letters*, 264(1), 245–258. <https://doi.org/10.1016/j.epsl.2007.09.035>
- Saucedo, G. J., & Wagner, D. L. (1992). *Geologic map of the Chico quadrangle*. Division of Mines and Geology.
- Slim, M., Perron, J. T., Martel, S. J., & Singha, K. (2015). Topographic stress and rock fracture: A two-dimensional numerical model for arbitrary topography and preliminary comparison with borehole observations. *Earth Surface Processes and Landforms*, 40(4), 512–529. <https://doi.org/10.1002/esp.3646>
- Trabucco, A., & Zomer, R. (2019). *Global aridity index and potential evapotranspiration (ET₀) climate database v2*. CGIAR Consortium for Spatial Information (CGIAR-CSI). Published online. available from the CGIAR-CSI GeoPortal at <https://cgiiarcsi.community>

- Wakabayashi, J., & Sawyer, T. L. (2000). Neotectonics of the Sierra Nevada and the Sierra Nevada-Basin and Range transition, California, with field trip stop descriptions for the northeastern Sierra Nevada. In E. R. Brooks, & L. T. Dida (Eds.), *Field Guide to the Geology and Tectonics of the Northern Sierra Nevada* (pp. 173–212). California Division of Mines and Geology.
- Wood, R. (2013). *Transient hillslope response to an incision wave sweeping up a watershed: A case study from the Salmon River*, MS thesis (pp. 42). San Jose State University.